Impacts of substrate conditions and post-annealing on monolayer iron-based superconductors

Guanyang He,[1] Yu Li,[1] Yuxuan Lei,[1,2] Xingyue Wang ®,[3] Minghu Pan ®,[3,*] and Jian Wang ®[1,2,4,5,†]

[1]*International Center for Quantum Materials, School of Physics, Peking University, Beijing 100871, China*
[2]*Beijing Academy of Quantum Information Sciences, Beijing 100193, China*
[3]*School of Physics and Information Technology, Shaanxi Normal University, Xi'an 710119, China*
[4]*Collaborative Innovation Center of Quantum Matter, Beijing 100871, China*
[5]*Hefei National Laboratory, Hefei 230088, China*

High-temperature superconductivity in monolayer FeSe/Fe(Te, Se) grown on $SrTiO_3$ (STO) substrates is closely related to the interface effects from STO. Using *in situ* low-temperature scanning tunneling microscopy/spectroscopy, we study the surface flatness and reconstructions of STO from different pre-treatment methods, and the influence of STO reconstructions on the interfacial superconductivity. Besides, the impacts from postgrowth annealing conditions on the morphology and superconducting properties of monolayer FeSe/Fe(Te, Se) are investigated. These results pave the way for the growth of high-temperature interface superconductors in a detailed level, and provide useful references for better interfacial engineering to foster superconductivity.

I. INTRODUCTION

The growth of monolayer FeSe on $SrTiO_3$ (STO) substrates leads to a significant breakthrough in both condensed matter physics and materials science for the greatly enhanced superconductivity. Comparing to FeSe films grown on graphene and bulk FeSe with superconducting gaps of 2–3 meV [1,2], the superconducting gap of monolayer FeSe/STO is raised to 15–20 meV [3,4] by the interfacial effects from STO. Electron doping from STO to FeSe alters the electronic structure of FeSe [5,6], and the surface phonons of STO couple with FeSe electrons [7,8], both considered to be the causes of boosted superconductivity. Recently, the zero-resistance temperature T_c^0 of monolayer FeSe on STO has been reported to be enhanced by doping Eu/Al at the interface [9], manifesting the importance of the interface. In order to fully exploit such interfacial engineering on the superconducting states in FeSe, the optimization of surface conditions of STO is necessary. The first factor is the surface flatness. Due to the Se-rich growth condition of FeSe in molecular beam epitaxy (MBE), excessive Se atoms trapped at the FeSe/STO interface may impair the interfacial phonon coupling and thus suppress the superconductivity [10,11]. A flatter STO surface with fewer atomic defects or vacancies might help to relieve this Se trapping. Besides, different surface reconstructions of the substrates also affect the superconducting properties of FeSe [12], since these reconstructions usually differ in the binding energy with FeSe and the oxygen vacancy concentration [13,14]. After the deposition of FeSe film on STO, postgrowth annealing

is usually required to tune the film stoichiometry and quality [5,10,15].

In this work, by utilizing scanning tunneling microscopy/spectroscopy (STM/S) and atomic force microscopy (AFM), we optimize the surface conditions of STO substrates by employing different pretreatment methods. The influence of STO surface reconstructions on the superconducting monolayer FeSe is revealed in detail. For the postgrowth annealing process, overannealing is exhibited to impair the superconductivity in monolayer FeSe/STO. In the fabrication of Fe(Te, Se)/STO as an important candidate of topological superconductor [16], the change of sample morphology upon postgrowth annealing is shown to be closely related to the emergence of superconducting phase.

II. MATERIALS AND METHODS

The experiments are mainly carried out in an ultrahigh vacuum (UHV) (1×10^{-10} mBar) MBE system combined with a low temperature STM/S at 4.3 K (Scienta Omicron, Inc.). The dI/dV spectra is measured by a polycrystalline Pt/Ir tip and standard lock-in technique, where the modulation voltage on the tip is 1 mV with the frequency of 1.769 kHz. The setups of STS measurements are $V = 40$ mV, $I = 2.5$ nA for dI/dV spectra unless otherwise stated, and $V = 1$ V, $I = 0.2$ nA for topographic images. The AFM measurements (Bruker, Corp.) are carried out in air at room temperature by silicon tip on nitride cantilever (tip model: SCANASYST-AIR). FeSe and Fe(Te, Se) monolayers are epitaxially grown on Nb-doped STO (wt % 0.7) for STM/S measurements or undoped STO substrates for transport. STO substrates are first chemically etched by 10% HCl solution in order to remove SrO termination and form a fully TiO_2-terminated surface [17,18]. Then, Nb-doped STO is pretreated *in situ* in the MBE chamber for

*Corresponding author: minghupan@snnu.edu.cn
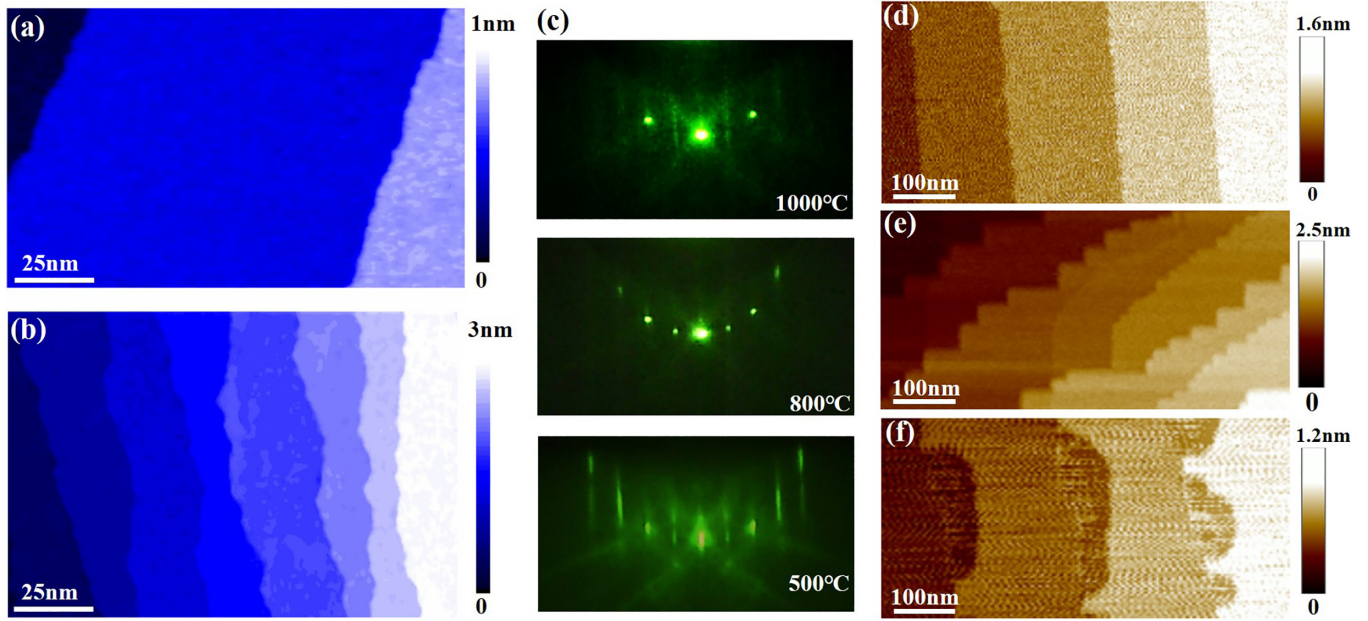†Corresponding author: jianwangphysics@pku.edu.cn

FIG. 1. (a), (b) STM topographies at 4.3 K of the Nb-doped STO annealed at 1000 °C with a cooling rate of 3 °C/min and 1.5 °C/min, respectively. (c) RHEED patterns of the STO in (a) at different temperatures during the cooling process. (d)–(f) AFM topographies of the undoped STO with the pre-treatment conditions of 1000 °C annealing and 2 °C/min cooling rate, 1000 °C annealing and 5.6 °C/min cooling rate, and an excessive annealing temperature of 1150 °C and 2 °C/min cooling rate, respectively.

30 min by either Se flux etching [6,19,20] or directly annealing [7,10] prior to the film growth. Undoped insulating STO is *ex situ* annealed under oxygen atmosphere in a tube furnace, preventing oxygen vacancies that generate unwanted conductive electrons on STO [17,21,22]. After that, undoped STO is exposed to air for few hours, followed by an *in situ* overnight degassing at 400 °C in the MBE chamber before film growth. FeSe/Fe(Te, Se) monolayers are deposited onto STO by co-evaporating high-purity Fe (99.994%) from an electron beam evaporator, and Te (99.999%), Se (99.999%) from standard Knudsen cells (K cell). The acceleration voltage and emission current of the electron beam evaporator are 800 V and 30 mA. For FeSe deposition, the K-cell temperature of Se is 155 °C, with the STO substrate temperature $T_{sub} = 430$ °C. For Fe(Te, Se) deposition, the K-cell temperatures of Se and Te are 130 °C and 250 °C respectively, with $T_{sub} = 350$ °C. Before STM/S measurements, the as-grown film is post-annealed with different conditions to be discussed later.

III. RESULTS AND DISCUSSION

Figure 1(a) is the STM topographic image of Nb-doped STO substrates treated by direct annealing in UHV, where the step-terrace structure is formed after the substrate cools down to room temperature from the annealing temperature of 1000 °C. The width of the individual terrace is around 100 nm, corresponding to a cooling rate of 3 °C/min. When the cooling rate is set to be as low as 1.5 °C/min, the terrace width becomes less than 20 nm [Fig. 1(b)], which is too narrow to grow a large area of homogeneous film. During the cooling process, the substrate is characterized by reflection high-energy electron diffraction (RHEED) at multiple temperatures, as shown in Fig. 1(c). The diffraction spots

become sharper and more streaklike as the temperature goes down, indicating the formation of an atomically flat surface with good crystallinity [23]. For the undoped insulating STO substrates, the sample morphologies are characterized by AFM images [Figs. 1(d)–1(f)]. To obtain a good terrace
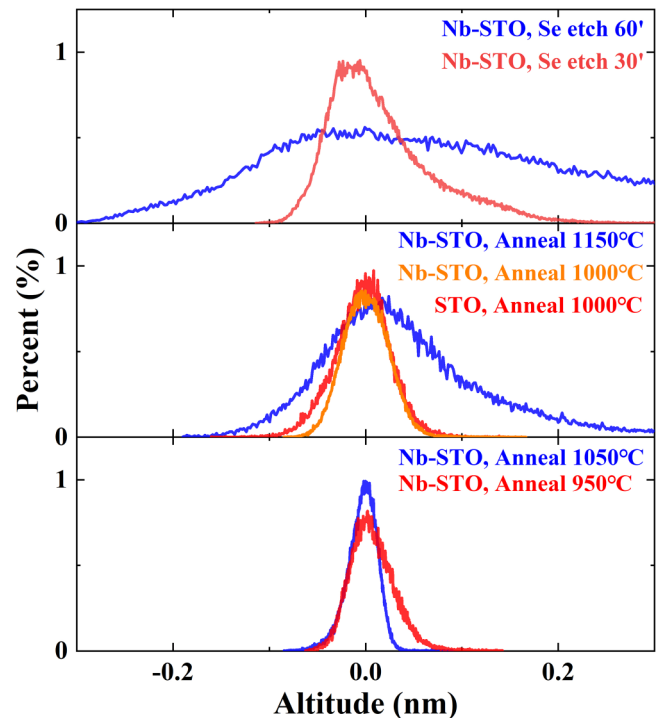

FIG. 2. Altitude distributions within a single terrace of STO surfaces from different pretreatment methods.
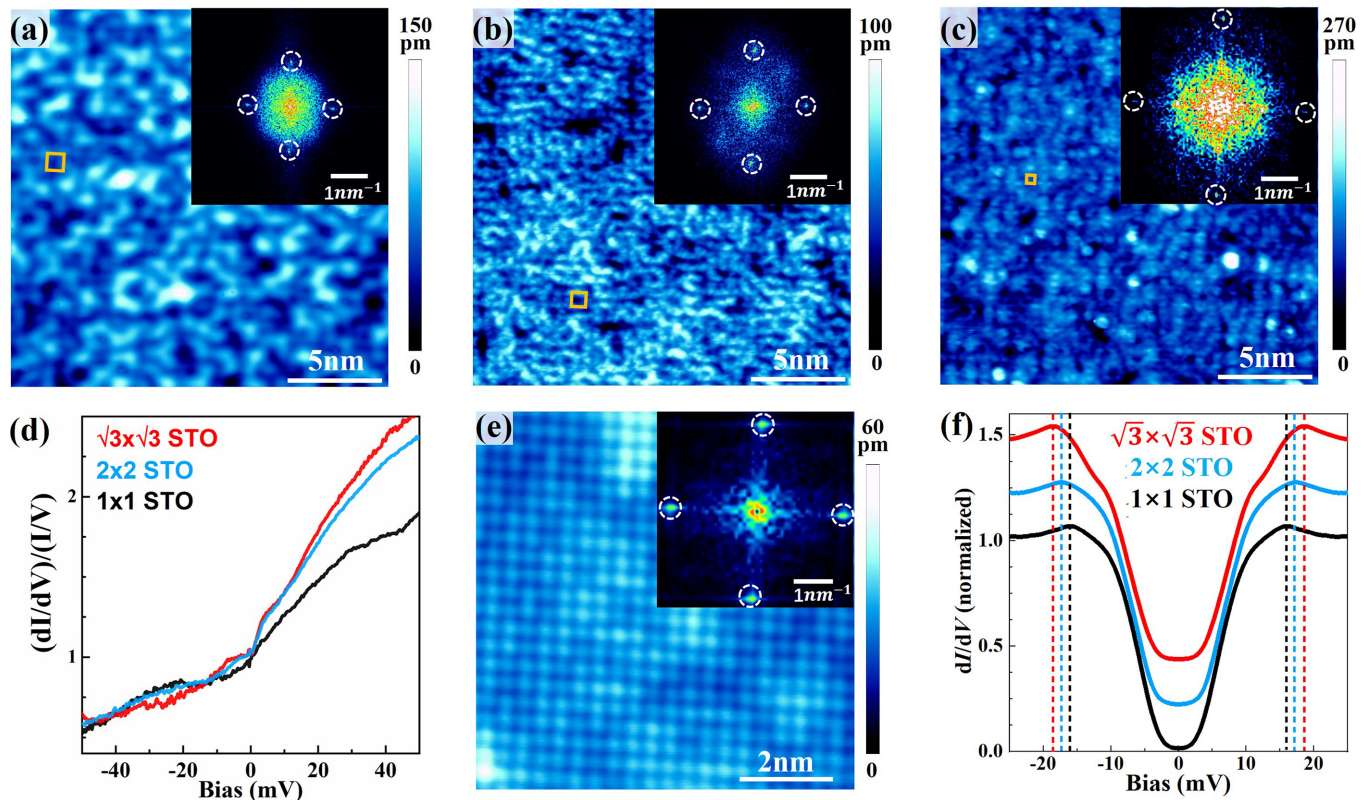
FIG. 3. (a)–(c) STM topographies of Nb-doped STO substrates annealed at $1000\,°C$, $1050\,°C$, or $950\,°C$, with corresponding FT images in the upper-right insets. White circles in the insets indicate the periodicities of 2×2, $\sqrt{3} \times \sqrt{3}$, or 1×1 surface reconstruction, respectively, and the orange squares denote the unit cells. (d) $(dI/dV)/(I/V)$ spectra of the STO surface with different reconstructions. (e) Typical STM topography of monolayer FeSe grown on $\sqrt{3} \times \sqrt{3}$ STO surface reconstruction. (f) Normalized dI/dV spectra of FeSe monolayers grown on three STO surface with different reconstructions. The spectra are vertically offset for clarity, and the positions of superconducting coherence peaks are denoted by dashed lines with one-to-one color correspondences to the curves.

structure similar to Fig. 1(a), a cooling rate of $2\,°C/min$ turns out to be appropriate for undoped STO, and the corresponding terrace is shown in Fig. 1(d). A large cooling rate ($5.6\,°C/min$) makes the terrace of undoped STO flawed with jagged edges as shown in Fig. 1(e). In addition, when the annealing temperature is raised from $1000\,°C$ to $1150\,°C$, two kinds of regions in bright/dark contrast appear on each terrace [Fig. 1(f)], indicating an undesirable coexistence of SrO and TiO_2 surface terminations [24]. A single TiO_2-terminated surface is preferred for the growth of superconducting FeSe, since the Ti-O bonds may support phonon interactions with FeSe [5,25].

By using the proper cooling rates ($3\,°C/min$ for Nb-doped STO, $2\,°C/min$ for undoped STO), well-defined step-terrace structures are generated. After direct annealing at various temperatures from $950\,°C$ to $1150\,°C$, or Se flux etching at $950\,°C$, the surface morphologies of Nb-doped STO are measured within a single terrace where a continuous film can be deposited (see STM morphology images in Fig. S2 of the Supplemental Material [26]). The altitude distributions of these morphologies are summarized in Fig. 2. It shows the percentage of each value of altitude on the STO surface, where a more concentrated distribution indicates a flatter surface. Se flux etching was reported to be capable of removing defects on STO [20], but in this work the surface flatness from this

treatment is slightly inferior to those from direct annealing at $950 - 1050\,°C$. Increasing the Se flux etching time from 30 to 60 min deteriorates the surface even more, thus direct annealing turns out a preferable pretreatment to get a better surface. Note that direct annealing at an excessive temperature ($1150\,°C$) is also detrimental to the surface flatness. Undoped STO substrate directly annealed at $1000\,°C$ shows good surface flatness as well.

Since the Nb-doped STO from direct annealing at $950 - 1050\,°C$ shows the least surface roughness, such treatment will be used for the next part of this paper. The Fourier transforms (FTs) from the surface morphologies of these substrates exhibit different periodicities. From Figs. 3(a)–3(c), the surface morphologies and corresponding FT images (upper-right insets) of STO annealed at $1000\,°C$, $1050\,°C$, and $950\,°C$ reflect different periodicities of 0.77, 0.67, and 0.39 nm, respectively. These periodicities correspond to the 2×2, $\sqrt{3} \times \sqrt{3}$, and 1×1 surface reconstruction of STO. Although numerous surface reconstructions have been reported previously on $SrTiO_3$ surface [12,19], the $\sqrt{3} \times \sqrt{3}$ periodicity has not been reported yet and its structure is unclear. Furthermore, we use $(dI/dV)/(I/V)$ instead of dI/dV to represent the density of states (DOS) of each reconstruction, in order to get rid of the STM setup effect [27,28]. The $(dI/dV)/(I/V)$ spectra of these three reconstructions are shown in Fig. 3(d). Each
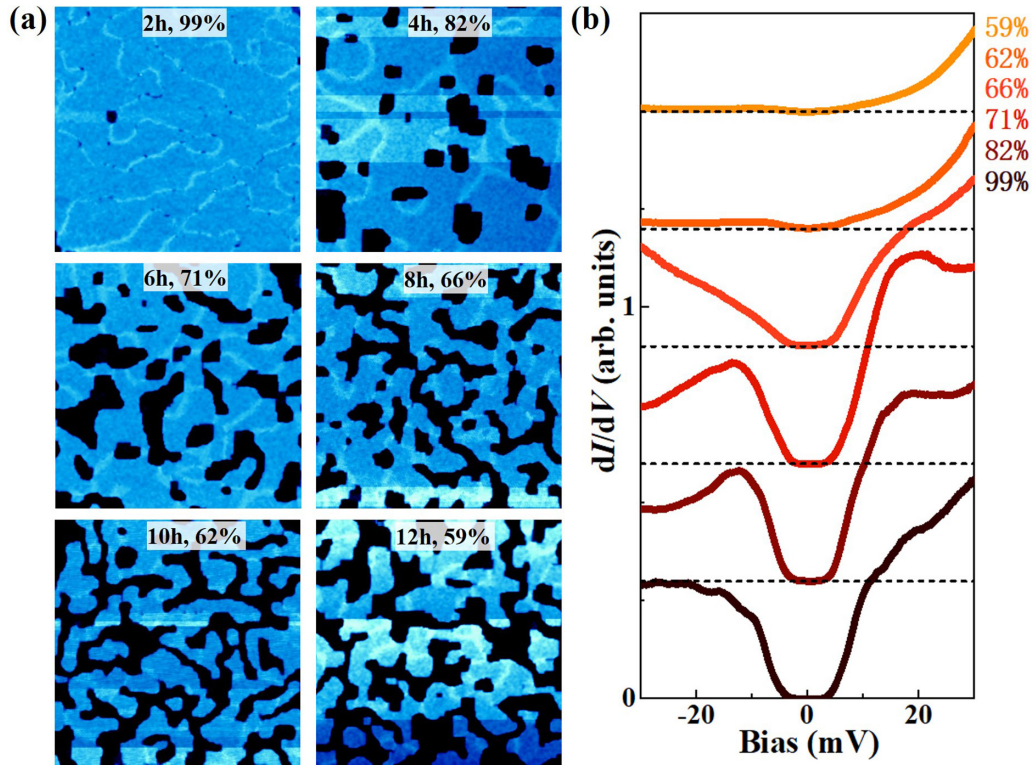
FIG. 4. (a) Evolution of STM topography of monolayer FeSe in consecutive postgrowth annealing periods. Each topographic image is $180 \times 180 \, \text{nm}^2$ with the film coverage labeled in percent (%) and annealing time labeled in hour (h), where the annealing time increases from top-left to bottom right. (b) dI/dV spectra measured on monolayer FeSe with different film coverages as shown in (a), vertically offset for clarity. Every dashed line indicates the position of $dI/dV = 0$ for each spectrum.

spectrum is averaged from two STO samples of the same reconstruction [see the STS spectra of each STO in Fig. S3(d) [26]]. Among these, the spectrum of $\sqrt{3} \times \sqrt{3}$ reconstruction shows the highest DOS in the positive biases, while the 1×1 reconstruction shows the lowest.

Next, FeSe monolayers are deposited onto these substrates under the same growth conditions described in Sec. II, and post-annealing is performed at $500\,^\circ\text{C}$ for 2 h. No clear difference is found in the morphologies of monolayer FeSe grown with different STO reconstructions, presenting the 0.38-nm lattice periodicity of FeSe. The morphology of monolayer FeSe grown on $\sqrt{3} \times \sqrt{3}$ reconstructed STO is shown in Fig. 3(e) [see Figs. S4(a) and S4(b) for FeSe on other STO reconstructions [26]]. The dI/dV spectra manifesting the superconducting gaps of monolayer FeSe on different STO surface reconstructions are measured [Fig. 3(f)], where each spectrum is averaged from two FeSe/STO samples with same STO surface reconstruction (see the STS spectra of each FeSe/STO sample in Fig. S6). Note that the spectra are normalized and symmetrized in order to compare between different reconstructed STO samples (see the data processing method in Fig. S5).

Monolayer FeSe as a multiband superconductor can exhibit double-gap feature in the spectra, ascribed to two electron pockets at the M point of the Brillouin zone [29,30]. In our case, we focus on the larger superconducting gap near 16 meV corresponding to the outer pocket, because the coherence peak from the smaller gap is often obscure in our spectra. Note also

that we use the position of the coherence peak to generally estimate the gap size, for the reason that the peak represents the maxima of an anisotropic gap in momentum space [31]. The position of coherence peaks can be determined by the zero points of dI^2/dV^2 curves [32] (see dI^2/dV^2 curves in Fig. S8), denoted by the dashed lines in Fig. 3(f) with one-to-one color correspondences. The distance between two coherence peaks gives the superconducting gap 2Δ, and $\Delta \approx 16.0, 17.1, 18.6$ meV can be estimated for 1×1, 2×2, $\sqrt{3} \times \sqrt{3}$ reconstructions, respectively. Instead of extracting Δ from the averaged spectra, we also extract Δ from each individual spectrum (see Fig. S7). The latter gives the statistical averages of the gap size $\bar{\Delta} \approx 15.8, 16.8, 18.2$ meV with standard deviations $\sigma \approx 1.0, 1.2, 1.1$ meV for 1×1, 2×2, $\sqrt{3} \times \sqrt{3}$ reconstruction, respectively. The correlation between the DOS of STO in Fig. 3(d) and Δ of monolayer FeSe in Fig. 3(f) suggests that the superconductivity of monolayer FeSe could be tuned by STO surface reconstructions, which may be attributed to different capability of electron transferring from reconstructed STO surface to FeSe. Since STO with $\sqrt{3} \times \sqrt{3}$ reconstruction leads to the largest Δ of monolayer FeSe, this type of substrate is used for our postgrowth annealing studies described in the next section.

Apart from the impact from STO substrates, the superconductivity of monolayer FeSe is subject to the postgrowth annealing process as well. Note that common annealing temperatures of monolayer FeSe near $500\,^\circ\text{C}$ [3,20,33] already exceed the temperature of film decomposition [5], so it
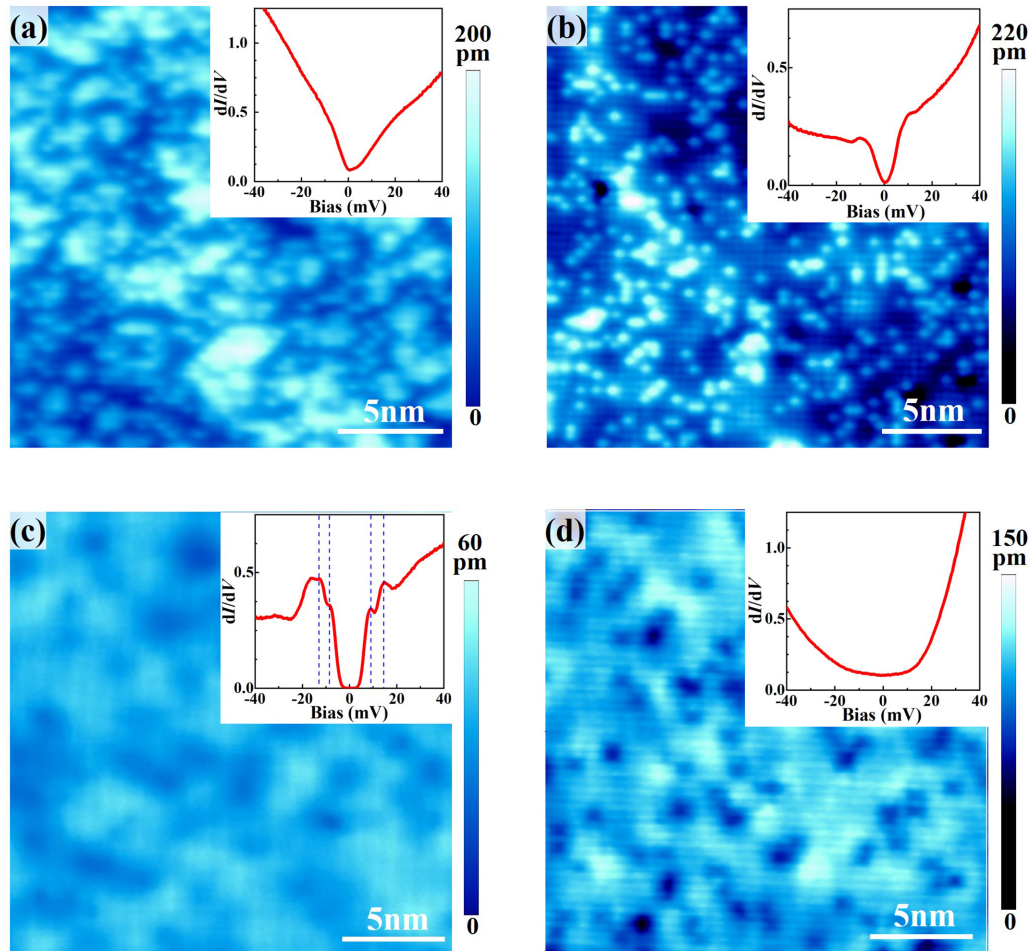
FIG. 5. (a)–(d) Surface morphologies and dI/dV spectra of monolayer Fe(Te, Se)/STO from postgrowth annealing at $330\,^\circ$C, $380\,^\circ$C, $430\,^\circ$C, $480\,^\circ$C, respectively. Superconducting coherence peaks appear in the spectrum in (c) as indicated by dashed lines.

is important to be wary of overannealing. To demonstrate the influence of overannealing, superconducting monolayer FeSe/STO is consecutively annealed at $500\,^\circ$C for 2 h at a time, and the evolution of its topography and superconducting property is characterized by STM/S. The film coverage keeps decreasing in the subsequent annealing periods, from 99% to 59% as shown by the time-lapsed series of STM images in Fig. 4(a). Overannealing indeed enlarges the holes on the surface and broadens the domain walls, while the surface atomic arrangement of FeSe keeps intact after annealing [Fig. S4(c)]. The dI/dV spectra of this monolayer FeSe under consecutive annealing are measured only on the undamaged regions and are present in Fig. 4(b), in which the superconducting gap disappears after 10 h post-annealing. Clearly, the overannealing turns FeSe monolayer into the nonsuperconducting state [12,34], or deteriorates the sample quality [35].

Monolayer FeSe/STO in this work reaches the superconducting state after postgrowth annealing at $500\,^\circ$C [Fig. 3(f)], although other annealing temperatures from $450\,^\circ$C to $600\,^\circ$C are also reported in the literature [11,17,36]. For Fe(Te, Se) as the close cousin of FeSe, the appropriate range of annealing temperature turns out much narrower according to our experiments. Four as-grown monolayer Fe(Te, Se)/STO samples (the growth method is described in Sec. II) are post-

annealed for 2 h at different temperatures, and then measured by STM/S. The thickness of our monolayer Fe(Te, Se) films is around 0.58 nm, indicating a Te concentration around 40% [37]. When the annealing temperature is $330\,^\circ$C [Fig. 5(a)], two kinds of surface protrusions randomly distribute on the surface with bright and dark contrast, which are likely Te (bright) and Se (dark) atoms clustering separately in the topmost atomic layer of Fe(Te, Se) [38,39]. The dI/dV spectrum (upper-right panel) measured on this surface shows no clear feature of superconductivity. For a higher annealing temperature of $380\,^\circ$C [Fig. 5(b)], the topmost Te/Se atoms become more dispersed. The height difference between two sites of atoms is 50–90 pm, larger than that reported in the literature (45 pm) [40], which might suggest that Te/Se atoms are not accommodated well into the same layer yet. The superconducting gap shows up despite its V shape and suppressed coherence peaks. When the annealing temperature rises to $430\,^\circ$C [Fig. 5(c)], The full superconducting gap is identified with two Δ values of 8.7 and 13.8 meV. Concomitantly, the surface morphology exhibits a small surface corrugation of height variation around 30 pm, indicating atomic-level uniformity of element distribution. Despite the variation in the DOS at different energies, the overall spectral shape and superconducting gap size are uniform rather than site-dependent, which

is reminiscent of the electronic homogeneity of monolayer Fe(Te, Se) [37]. Nevertheless, when annealing temperature is raised to 480 °C [Fig. 5(d)], many topmost Te/Se atoms are desorbed. The film becomes no longer superconducting and numerous deep pits and trenches with the depth of ~ 100 pm appear on the surface. Based on these results, a specific annealing temperature is crucial for the emergence of superconductivity in Fe(Te, Se), at which temperature Te/Se atoms blend well in one atomic layer to form a spatially homogeneous lattice.

IV. CONCLUSION

Multiple factors relevant to the growth of FeSe/Fe(Te, Se) on STO substrates are investigated in detail by *in situ* MBE and STM/S. The surface flatness of STO substrates from various pretreatment methods is explored, and the optimal flatness is obtained by direct annealing STO in a temperature window of $950 - 1050$ °C. In this window, three surface reconstructions of the Nb-doped STO, $\sqrt{3} \times \sqrt{3}$, 2×2, and 1×1, are observed with different DOSs at positive bias near the Fermi level. Monolayer FeSe grown on the Nb-doped STO reconstruction with higher DOS exhibits a larger superconducting gap, which can be attributed to a stronger electron doping effect. These findings illustrate the interfacial engineering on realizing and improving the superconducting states in monolayer FeSe. Besides, we further reveal that the superconducting properties of monolayer FeSe/Fe(Te, Se) change with different postgrowth annealing conditions. The surface morphology is shown to play a key role in the emergence of superconductivity during post-annealing, which sheds light on the understanding of high-temperature interface superconductivity.

[1] C.-L. Song, Y.-L. Wang, P. Cheng, Y.-P. Jiang, W. Li, T. Zhang, Z. Li, K. He, L. Wang, J.-F. Jia, H.-H. Hung, C. Wu, X. Ma, X. Chen, and Q. Xue, Direct observation of nodes and two fold symmetry in FeSe superconductor, Science **332**, 1410 (2011).

[2] A. E. Böhmer and A. Kreisel, Nematicity, magnetism and superconductivity in FeSe, J. Phys.: Condens. Matter **30**, 023001 (2017).

[3] D. Huang and J. E. Hoffman, Monolayer FeSe on SrTiO$_3$, Annu. Rev. Condens. Matter Phys. **8**, 311 (2017).

[4] C. Liu and J. Wang, Heterostructural one-unit-cell FeSe/SrTiO$_3$: From high-temperature superconductivity to topological states, 2D Mater. **7**, 022006 (2020).

[5] H. Zhang, D. Zhang, X. Lu, C. Liu, G. Zhou, X. Ma, L. Wang, P. Jiang, Q.-K. Xue, and X. Bao, Origin of charge transfer and enhanced electron–phonon coupling in single unit-cell FeSe films on SrTiO$_3$, Nat. Commun. **8**, 214 (2017).

[6] S. Tan, Y. Zhang, M. Xia, Z. Ye, F. Chen, X. Xie, R. Peng, D. Xu, Q. Fan, H. Xu, J. Jiang, T. Zhang, X. Lai, T. Xiang, and J. Hu, Binping Xie, and Donglai Feng, Interface-induced superconductivity and strain-dependent spin density waves in FeSe/SrTiO$_3$ thin films, Nat. Mater. **12**, 634 (2013).

[7] J. J. Lee, F. T. Schmitt, R. G. Moore, S. Johnston, Y.-T. Cui, W. Li, M. Yi, Z. K. Liu, M. Hashimoto, Y. Zhang, D. H. Lu, T. P. Devereaux, D. H. Lee, and Z. X. Shen, Interfacial mode coupling as the origin of the enhancement of Tc in FeSe films on SrTiO$_3$, Nature (London) **515**, 245 (2014).

[8] S. Zhang, J. Guan, X. Jia, B. Liu, W. Wang, F. Li, L. Wang, X. Ma, Q. Xue, J. Zhang, E. W. Plummer, X. Zhu, and J. Guo, Role of SrTiO$_3$ phonon penetrating into thin FeSe films in the enhancement of superconductivity, Phys. Rev. B **94**, 081116(R) (2016).

[9] X. Jiao, W. Dong, M. Shi, H. Wang, C. Ding, Z. Wei, G. Gong, Y. Li, Y. Li, B. Zuo, J. Wang, D. Zhang, M. Pan, L. Wang, and Q.-K. Xue, Significantly enhanced superconductivity in monolayer FeSe films on SrTiO$_3$ (001) via metallic δ-doping, Natl. Sci. Rev. nwad213 (2023).

[10] X. Jiao, G. Gong, Z. Zhang, W. Dong, C. Ding, M. Pan, L. Wang, and Q.-K. Xue, Post-growth Fe deposition on the superconductivity of monolayer FeSe films on SrTiO$_{3-\delta}$, Phys. Rev. Mater. **6**, 064803 (2022).

[11] F. Li, Q. Zhang, C. Tang, C. Liu, J. Shi, C. N. Nie, G. Zhou, Z. Li, W. Zhang, C.-L. Song, K. He, S. Ji, S. Zhang, L. Gu, L. Wang, X. Ma, and Q. Xue, Atomically resolved FeSe/SrTiO$_3$ (001) interface structure by scanning transmission electron microscopy, 2D Mater. **3**, 024002 (2016).

[12] T. Tanaka, K. Akiyama, S. Ichinokura, R. Shimizu, T. Hitosugi, and T. Hirahara, Superconducting dome revealed by surface structure dependence in single unit cell FeSe on SrTiO$_3$ (001), Phys. Rev. B **101**, 205421 (2020).

[13] J. Bang, Z. Li, Y. Y. Sun, A. Samanta, Y. Y. Zhang, W. Zhang, L. Wang, X. Chen, X. Ma, Q.-K. Xue, and S. B. Zhang, Atomic and electronic structures of single-layer FeSe on SrTiO$_3$ (001): The role of oxygen deficiency, Phys. Rev. B **87**, 220503(R) (2013).

[14] R. Di Capua, M. Radovic, G. M. De Luca, I. Maggio-Aprile, F. Miletto Granozio, N. C. Plumb, Z. Ristic, U. Scotti Di Uccio, R. Vaglio, and M. Salluzzo, Observation of a two-dimensional electron gas at the surface of annealed SrTiO$_3$ single crystals by scanning tunneling spectroscopy, Phys. Rev. B **86**, 155425 (2012).

[15] C. Liu and K. Zou, Tuning stoichiometry and its impact on superconductivity of monolayer and multilayer FeSe on SrTiO$_3$, Phys. Rev. B **101**, 140502(R) (2020).

[16] N. Hao and J. Hu, Topological quantum states of matter in iron-based superconductors: From concept to material realization, Natl. Sci. Rev. **6**, 213 (2019).

[17] W. Zhang, Z. Li, F. Li, H. Zhang, J. Peng, C. Tang, Q. Wang, K. He, X. Chen, L. Wang, X. Ma, and Q. K. Xue, Interface

charge doping effects on superconductivity of single-unit-cell FeSe films on SrTiO$_3$ substrates, Phys. Rev. B **89**, 060506(R) (2014).

[18] M. Kareev, S. Prosandeev, J. Liu, C. Gan, A. Kareev, J. W. Freeland, M. Xiao, and J. Chakhalian, Atomic control and characterization of surface defect states of TiO$_2$ terminated SrTiO$_3$ single crystals, Appl. Phys. Lett. **93**, 061909 (2008).

[19] T. Tanaka, K. Akiyama, R. Yoshino, and T. Hirahara, Superconductivity of single unit cell FeSe/SrTiO$_3$ (001): Substrate-surface superstructure dependence, Phys. Rev. B **98**, 121410(R) (2018).

[20] Q.-Y. Wang, Z. Li, W.-H. Zhang, Z.-C. Zhang, J.-S. Zhang, W. Li, H. Ding, Y. Ou, P. Deng, K. Chang, J. Wen, C. Song, K. He, J. F. Jia, S. Ji, Y. Wang, L. Wang, X. Chen, X. Ma, and Q. Xue, Interface-induced high-temperature superconductivity in single unit-cell FeSe films on SrTiO$_3$, Chin. Phys. Lett. **29**, 037402 (2012).

[21] W.-H. Zhang, Y. Sun, J.-S. Zhang, F.-S. Li, M.-H. Guo, Y.-F. Zhao, H.-M. Zhang, J.-P. Peng, Y. Xing, H.-C. Wang, T. Fujita, A. Hirata, Z. Li, H. Ding, C. Tang, M. Wang, Q. Wang, K. He, S. Ji, X. Chen *et al.*, Direct observation of high-temperature superconductivity in one-unit-cell FeSe films, Chin. Phys. Lett. **31**, 017401 (2014).

[22] W. Zhao, M. Li, C.-Z. Chang, J. Jiang, L. Wu, C. Liu, J. S. Moodera, Y. Zhu, and M. H. W. Chan, Direct imaging of electron transfer and its influence on superconducting pairing at FeSe/SrTiO$_3$ interface, Sci. Adv. **4**, eaao2682 (2018).

[23] B. D. Faeth, S.-L. Yang, J. K. Kawasaki, J. N. Nelson, P. Mishra, C. T. Parzyck, C. Li, D. G. Schlom, and K. M. Shen, Incoherent Cooper pairing and pseudogap behavior in single-layer FeSe/SrTiO$_3$, Phys. Rev. X **11**, 021054 (2021).

[24] F. Gellé, R. Chirita, D. Mertz, M. V. Rastei, A. Dinia, and S. Colis, Guideline to atomically flat TiO$_2$-terminated SrTiO$_3$ (001) surfaces, Surf. Sci. **677**, 39 (2018).

[25] S. N. Rebec, T. Jia, C. Zhang, M. Hashimoto, D.-H. Lu, R. G. Moore, and Z.-X. Shen, Coexistence of replica bands and superconductivity in FeSe monolayer films, Phys. Rev. Lett. **118**, 067002 (2017).

[26] See Supplemental Material at http://link.aps.org/supplemental/10.1103/PhysRevMaterials.8.014802 for more detailed information supporting the discussions in the main text.

[27] Y. Hasegawa and Ph. Avouris, Direct observation of standing wave formation at surface steps using scanning tunneling spectroscopy, Phys. Rev. Lett. **71**, 1071 (1993).

[28] R. J. Hamers, Atomic-resolution surface spectroscopy with the scanning tunneling microscope, Annu. Rev. Phys. Chem. **40**, 531 (1989).

[29] Q. Fan, W. H. Zhang, X. Liu, Y. J. Yan, M. Q. Ren, R. Peng, H. C. Xu, B. P. Xie, J. P. Hu, T. Zhang, and D. L. Feng, Plain s-wave superconductivity in single-layer FeSe on SrTiO$_3$

probed by scanning tunnelling microscopy, Nat. Phys. **11**, 946 (2015).

[30] Y. Yamakawa and H. Kontani, Superconductivity without a hole pocket in electron-doped FeSe: Analysis beyond the Migdal-Eliashberg formalism, Phys. Rev. B **96**, 045130 (2017).

[31] P. O. Sprau, A. Kostin, A. Kreisel, A. E. Böhmer, V. Taufour, P. C. Canfield, S. Mukherjee, P. J. Hirschfeld, B. M. Andersen, and J. C. Séamus Davis, Discovery of orbital-selective Cooper pairing in FeSe, Science **357**, 75 (2017).

[32] C. Liu, Z. Wang, S. Ye, C. Chen, Y. Liu, Q. Wang, Q.-H. Wang, and J. Wang, Detection of bosonic mode as a signature of magnetic excitation in one-unit-cell FeSe on SrTiO$_3$, Nano Lett. **19**, 3464 (2019).

[33] Q. Wang, W. Zhang, Z. Zhang, Y. Sun, Y. Xing, Y. Wang, L. Wang, X. Ma, Q.-K. Xue, and J. Wang, Thickness dependence of superconductivity and superconductor–insulator transition in ultrathin FeSe films on SrTiO$_3$ (001) substrate, 2D Mater. **2**, 044012 (2015).

[34] W. H. Zhang, X. Liu, C. H. P. Wen, R. Peng, S. Y. Tan, B. P. Xie, T. Zhang, and D. L. Feng, Effects of surface electron doping and substrate on the superconductivity of epitaxial FeSe films, Nano Lett. **16**, 1969 (2016).

[35] S. He, J. He, W. Zhang, L. Zhao, D. Liu, X. Liu, D. Mou, Y.-B. Ou, Q.-Y. Wang, Z. Li, L. Wang, Y. Peng, Y. Liu, C. Chen, L. Yu, G. Liu, X. Dong, J. Zhang, C. Chen, Z. Xu, X. Chen, X. Ma, Q. Xue, and X. J. Zhou, Phase diagram and electronic indication of high-temperature superconductivity at 65 K in single-layer FeSe films, Nat. Mater. **12**, 605 (2013).

[36] D. Huang, C.-L. Song, T. A. Webb, S. Fang, C.-Z. Chang, J. S. Moodera, E. Kaxiras, and J. E. Hoffman, Revealing the empty-state electronic structure of single-unit-cell FeSe/SrTiO$_3$, Phys. Rev. Lett. **115**, 017002 (2015).

[37] F. Li, H. Ding, C. Tang, J. Peng, Q. Zhang, W. Zhang, G. Zhou, D. Zhang, C.-L. Song, K. He, S. Ji, X. Chen, L. Gu, L. Wang, X. C. Ma, and Q. K. Xue, Interface-enhanced high-temperature superconductivity in single-unit-cell FeTe$_{1-x}$Se$_x$ films on SrTiO$_3$, Phys. Rev. B **91**, 220503(R) (2015).

[38] C. Chen, K. Jiang, Y. Zhang, C. Liu, Y. Liu, Z. Wang, and J. Wang, Atomic line defects and zero-energy end states in monolayer Fe (Te, Se) high-temperature superconductors, Nat. Phys. **16**, 536 (2020).

[39] Z. Wei, C. Ding, Y. Sun, L. Wang, and Q.-K. Xue, Preparation of spatially uniform monolayer FeSe$_x$Te$_{1-x}$ ($0 < x \leqslant 1$) by topotactic reaction, Nano Res. **16**, 1712 (2023).

[40] X. He, G. Li, J. Zhang, A. B. Karki, R. Jin, B. C. Sales, A. S. Sefat, M. A. McGuire, D. Mandrus, and E. W. Plummer, Nanoscale chemical phase separation in FeTe$_{0.55}$Se$_{0.45}$ as seen via scanning tunneling spectroscopy, Phys. Rev. B **83**, 220502(R) (2011).